

# Quantum cooling below absolute zero

Francesco Libbi,<sup>1</sup> Lorenzo Monacelli,<sup>2</sup> and Boris Kozinsky<sup>1,3</sup>

<sup>1</sup>*John A. Paulson School of Engineering and Applied Sciences, Harvard University, Cambridge, MA 02138, USA\**

<sup>2</sup>*Department of Physics, Sapienza University of Rome, Piazzale Aldo Moro 5, 00185 Rome, Italy*

<sup>3</sup>*Robert Bosch LLC Research and Technology Center, Watertown, MA 02472, USA*

Similar to other perovskites in its family, SrTiO<sub>3</sub> exhibits a significant softening of the ferroelectric mode with decreasing temperature, a behavior that typically heralds the onset of a ferroelectric transition. However, this material remains paraelectric down to 0 K due to the Heisenberg quantum uncertainty principle that prevents atoms from localizing in the ferroelectric minima, a fundamental limit that appears impossible to overcome. This work shows that in the strong out-of-equilibrium regime induced by resonant mid-IR pulses, quantum fluctuations can be suppressed, effectively cooling the material below the 0 K ground state and inducing a ferroelectric transition in SrTiO<sub>3</sub> that is otherwise impossible. The appearance of a metastable state, that is distinct from the conventional ground state, is the first demonstration of how it is possible to leverage and control quantum fluctuations with pulsed light to qualitatively alter the free energy landscape of a quantum system. We predict the conditions and system parameter under which induced non-equilibrium state can be long-lived and even permanent. In providing a quantitative description, based on first principles machine learned potential energy surface, we explain recent experimental observations of light-induced ferroelectric transition in this material.

Quantum lattice fluctuations play a crucial role in shaping the equilibrium properties of many materials. For example, they stabilize the symmetric phase in H<sub>3</sub>S<sup>1</sup> and LaH<sub>10</sub><sup>2</sup>, enabling high-temperature superconductivity, and drive the metallization of hydrogen phase III at 380 GPa<sup>3</sup>. In perovskites, these fluctuations can stabilize the symmetric paraelectric phase by allowing nuclear wavefunction tunneling through the shallow barrier of the double-well potential energy surface (PES) of the ferroelectric (FE) soft mode<sup>4-7</sup>, a phenomenon known as quantum paraelectricity. Notable examples include KTaO<sub>3</sub><sup>5</sup> and SrTiO<sub>3</sub> (STO)<sup>4,6,7</sup>. STO, in particular, has been extensively studied due to its frustrated ground state, which arises from the competition between antiferrodistortive (AFD) and FE instabilities<sup>8</sup>. Below 110 K, the rotation of the AFD mode significantly flattens the PES of the FE soft mode<sup>9</sup>, facilitating quantum tunneling and thereby suppressing ferroelectric order.

The close proximity of STO to the ferroelectric transition renders it highly sensitive to external perturbations such as epitaxial strain<sup>10</sup>, oxygen isotope substitution<sup>11,12</sup>, or partial cation doping<sup>13</sup>, all of which can stabilize the ferroelectric phase. This inherent sensitivity suggests that dynamic modulation of quantum fluctuations induced by strong THz pulse irradiation may be the driving mechanism behind the ferroelectric transition observed in Refs.<sup>14,15</sup>.

The dramatic response of nuclear quantum fluctuations to nonequilibrium conditions remains largely unexplored. Recent studies have observed that irradiation of cubic STO with a strong mid-infrared pulse quenches lattice fluctuations in the AFD mode. This mechanism was proposed as a route to potentially stabilizing the ferroelectric phase<sup>9</sup>. However, there is no experimental evidence or atomistic simulations in support of this picture. Furthermore, the dynamics of quantum fluctuations associated with the FE mode, which are expected to play a key

role in driving the phase transition, remain entirely unexamined. A more comprehensive investigation is therefore required.

In this work, we present the first full-atomistic study of the dynamics of FE quantum fluctuations induced by a strong THz pulse. Our first principles investigation, accelerated by machine learning, predicts and comprehensively explains the light-induced ferroelectric transition reported in Ref.<sup>14</sup>. Specifically, we reveal that this transition is driven by the drastic cooling, or quenching, of FE quantum lattice fluctuations, which ultimately results in the self-trapping of the FE mode in the FE state. Remarkably, we demonstrate that under some conditions it is possible to stabilize this non-equilibrium metastable FE state, making it long-lived and even permanent.

Other proposed explanations for the light-induced ferroelectric transition have relied on the coupling between phonons and stress<sup>14</sup>. This appears to be the mechanism at play when the FE mode is driven directly<sup>16,17</sup>, as in the experiments reported in Ref.<sup>15</sup>. While certainly interesting, this type of transition can be understood within a semiclassical framework, through modifications of thermodynamic variables such as pressure. The mechanism we reveal in this work, by contrast, is fundamentally different. It is rooted in the dynamics of nuclear degrees of freedom that have no classical counterpart, representing a genuinely quantum phenomenon.

To achieve this, we employ a novel theoretical framework to describe the evolution of the full quantum fluctuation and the nuclear density matrix. This approach extends the recently developed time-dependent self-consistent harmonic approximation (TD-SCHA)<sup>18-20</sup> by incorporating an analytical framework for evaluating quantum ensemble averages. The framework is highly general, encompassing all phonon-phonon interactions up to fourth order, and is rigorously derived from first principles. A detailed derivation of the theory is provided in

Ref.<sup>21</sup>, with a summarized account included in the Methods section.

In our calculations, a 40-atom STO supercell is irradiated with a Gaussian mid-IR pulse of intensity 2000 kV/cm and frequency 16.0 THz, polarized along the (1,0,0) direction of the tetragonal STO cell, as represented in FIG. 1a. The pulse starts at approximately 200 fs and ends at around 1000 fs. Initially, the system is in thermodynamic equilibrium in the paraelectric ground state at 0 K.

The pulse selectively excites the high-frequency (15.5 THz) IR-active mode at  $\Gamma$ , whose dynamics is depicted in FIG. 1b, alongside that of the FE and AFD modes. The pumping field induces pronounced oscillations beyond the linear regime in the resonant IR active vibrational mode, with a peak amplitude of approximately  $0.3 \text{ \AA}\sqrt{\text{amu}}$ . Over time, the amplitude of these oscillations decreases as energy is redistributed to other phonons via anharmonic scattering. At approximately 4 ps (3.0 ps after the end of the pulse), the FE mode displays a rapid acceleration, ultimately reaching a ferroelectric configuration in which it becomes self-trapped. The transition into the ferroelectric state occurs exponentially in time, as witnessed by the linear displacement of the FE mode from the paraelectric position in semi-log scale (FIG. 1c). Concurrently, the AFD mode exhibits large chaotic oscillations. The FE mode continues to oscillate around the new minima with larger amplitudes than the pumped mid-IR mode. This is expected, as the elastic energy of a phonon mode scales with the square of its frequency. With a frequency approximately 30 times higher than the FE mode, the IR mode exhibits much smaller oscillations for the same energy.

To understand the origin of the laser-induced ferroelectric transition, we analyze the dynamics of the quantum fluctuations  $\mathcal{A}_\mu$  in the FE and AFD modes. These are defined as the quantum-averaged square displacement of phonons from their mean position  $\delta R_\mu$ ,  $\mathcal{A}_\mu = \langle \delta R_\mu^2 \rangle$ <sup>18–20</sup>. Corresponding to the steep increase of the FE coordinate, we observe a drastic drop of quantum fluctuations along the ferroelectric mode ( $\mathcal{A}_{FE}$ ), which localizes the atoms in the ferroelectric minima, stabilizing the ferroelectric phase. This behavior can be interpreted as a dynamical cooling of the nuclei, which suppresses quantum fluctuations below their equilibrium value at 0 K,  $\mathcal{A}_{FE}^{\text{eq}} = \frac{\hbar}{2\omega_{FE}} \simeq 0.37 \text{ \AA}^2\text{amu}$ , where  $\omega_{FE}$  is the equilibrium frequency of the soft mode. We can formulate a minimal model to show that the suppression of fluctuations is a consequence of the exponential growth of ferroelectricity (FIG. 1c). This model can be derived restricting the full quantum motion to only the ferroelectric dynamics (Sec I of Supplementary Information, SI<sup>22</sup>):

$$\begin{aligned} \ddot{\tilde{\mathcal{A}}}_{FE} + 4\dot{\tilde{\mathcal{A}}}_{FE} \left[ \omega_{FE}^2 + \frac{1}{2}\psi_{FE}(\tilde{\mathcal{R}}_{FE}^2 + \tilde{\mathcal{A}}_{FE}) \right] \\ + \psi_{FE}\mathcal{A}_{FE}(2\dot{\tilde{\mathcal{R}}}_{FE}\tilde{\mathcal{R}}_{FE} + \dot{\tilde{\mathcal{A}}}_{FE}) = 0 \end{aligned} \quad (1)$$

Here,  $\tilde{\mathcal{A}}_{FE} = \mathcal{A}_{FE} - \mathcal{A}_{FE}^{\text{eq}}$  and  $\tilde{\mathcal{R}}_{FE} = \mathcal{R}_{FE} - \mathcal{R}_{FE}^{\text{eq}}$  are the deviations of the quantum fluctuations and the

FE coordinate from their equilibrium values, respectively, and  $\psi_{FE} = \frac{\partial^4 V}{\partial \mathcal{R}_{FE}^4}$  is the fourth derivative of the PES of the FE mode at the symmetric configuration. Substituting the exponential growth of ferroelectricity  $\mathcal{R}_{FE} \sim \alpha e^{t/\tau}$ , we immediately derive the corresponding quenching of quantum fluctuations  $\mathcal{A}_{FE}(t) \simeq$

$$\mathcal{A}_{FE}^{\text{eq}} \left( 1 - \frac{\alpha^2 \tau^2 \psi_{FE}}{4\omega_{FE}^2 \tau^2 + \psi_{FE} \mathcal{A}_{FE}^{\text{eq}} \tau + 4} e^{2t/\tau} \right). \quad \text{Simultaneously,}$$

the momentum-momentum fluctuations increase following the Heisenberg uncertainty, as demonstrated in SI, Sec. II.

In a purely classical framework, where the nuclear density is sharply localized ( $\mathcal{A}_{FE} = 0$ ), the nuclei would settle in one of the minima of the double-well PES<sup>4,6,17</sup>, resulting in a ferroelectric state. However, quantum fluctuations spread the nuclear density across the potential barrier, enabling tunneling between the wells and stabilizing the paraelectric phase. Consequently, the cooling of the FE fluctuations drives the system toward the classical regime, abruptly stabilizing the ferroelectric state and leaving it self-trapped in the newly symmetry-broken phase.

Contrary to the common assumption<sup>23</sup>, we show that the pumped IR mode does not directly drive the ferroelectric transition, but rather couples to a nontrivial set of finite-momentum phonons that mediate the response. To this aim, we decompose the total force responsible for the ferroelectric drive  $f_{FE}$  into a harmonic drive, anharmonic part, and a pure quantum force:

$$\begin{aligned} f_{FE} = & - \overbrace{\sum_{\nu} \left\langle \frac{\partial^2 V}{\partial \mathcal{R}_{FE} \partial \mathcal{R}_{\nu}} \right\rangle \mathcal{R}_{\nu}}^{\text{harmonic}} + \\ & - \underbrace{\sum_{\nu\sigma\tau} \frac{1}{3!} \psi_{\nu\sigma\tau} \mathcal{R}_{\nu} \mathcal{R}_{\sigma} \mathcal{R}_{\tau}}_{\text{anharmonic}} - \overbrace{\sum_{\nu\sigma} \chi_{\nu\sigma} \mathcal{A}_{\nu\sigma}}^{\text{quantum}}. \end{aligned} \quad (2)$$

Here, the bracket notation  $\langle \cdot \rangle$  denotes the average over the nuclear quantum distribution, the coefficients  $\chi_{\mu\nu\sigma}$  and  $\psi_{\mu\nu\sigma\tau}$  represent the third- and fourth-order derivatives of the STO potential energy around the symmetric configuration (more details in the Methods section). The first term on the right-hand side corresponds to the generalized elastic force. The second term represents the classical anharmonic force of a symmetric quartic potential, while the last term accounts for a purely quantum force mediated by quantum fluctuations  $\mathcal{A}_{\nu\sigma} = \langle \delta R_{\nu} \delta R_{\sigma} \rangle$ . Notably, while harmonic and anharmonic terms account for phonon modes at  $\Gamma$  (where the third-order coefficients of the potential energy surface,  $\chi_{\mu\nu\sigma}$ , vanish by symmetry), the quantum fluctuations include contributions from all triplets of phonon modes  $\nu, \sigma$  whose momenta add up to a reciprocal lattice vector,  $\vec{q}_{\nu} + \vec{q}_{\sigma} = \vec{G}$ . FIG. 1e illustrates these three force components pro-

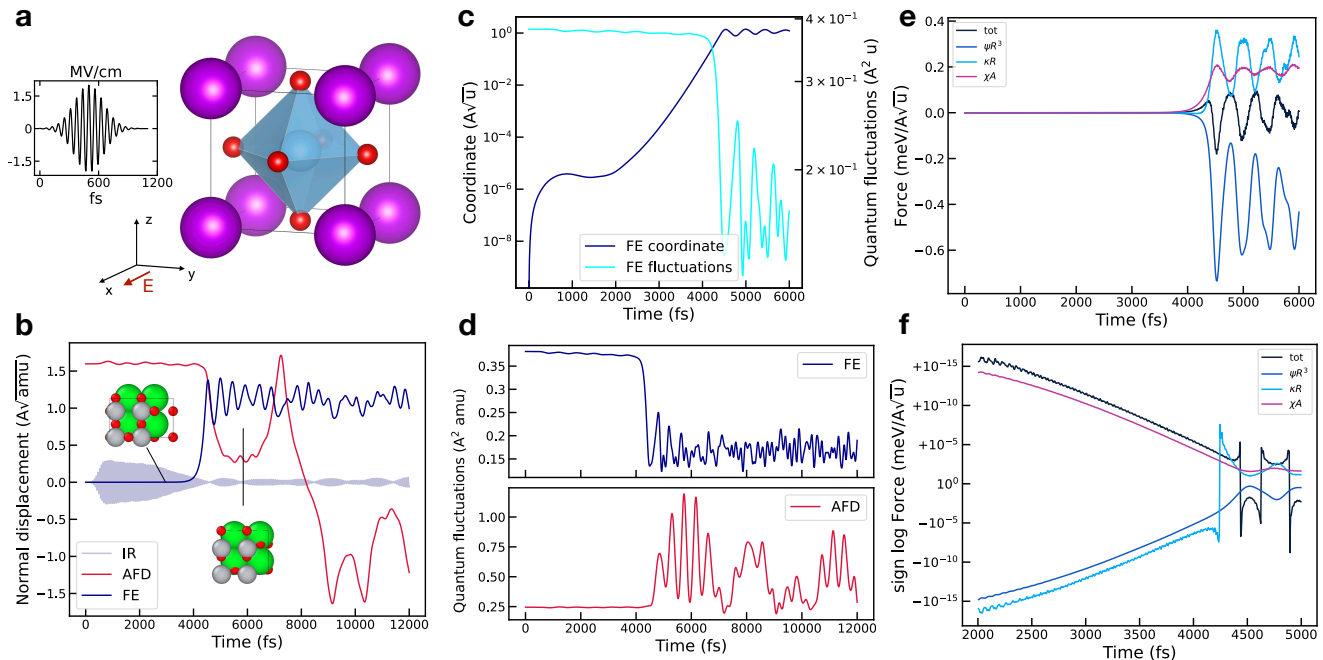


FIG. 1: **a** Schematic representation of the STO unit cell irradiated with a laser pulse. **b** Displacement of the FE, AFD, and IR modes as a function of time. **c** Logarithmic plot of the FE displacement and fluctuations. **d** FE and AFD fluctuations as a function of time. **e** Components of the force acting on the FE mode, with their signed logarithmic representation shown in **f**.

jected onto the FE mode, while FIG. 1f shows their signed logarithmic representation (negative values correspond to negative forces). From 1.5 ps to 3.5 ps, the total force acting on the FE mode increases exponentially, as evidenced by the linear trend in the logarithmic plot. During this time interval, the quantum force  $\chi\mathcal{A}$  dominates. Instead, the elastic component remains a restoring force until the ferroelectric transition, thus opposing the ferroelectricity. This observation leads us to conclude that it is not the cooling of quantum fluctuations that initially destabilizes the paraelectric system and drives the ferroelectric transition. Instead, the cooling is a consequence of the exponential motion and contributes to the system's instability only around 3.5 ps. This behavior also demonstrates that the FE mode is not directly excited by the IR mode. Instead, its activation occurs indirectly through scattering processes that populate off-diagonal components of the quantum fluctuations matrix. In particular, due to inversion symmetry in the paraelectric state, the coupling tensor  $\chi_{\mu\nu\sigma}$  vanishes when  $\mu, \nu, \sigma$  are zone-center modes, implying that only finite-momentum phonons can mediate this interaction.

Further analysis of the contributions from the various modes shows that no single pair of modes is responsible for the quantum force. Instead, the contribution is broadly distributed, consistent with a continuum of interacting modes. A schematic representation of the phenomenon is shown in FIG. 2a.

To determine whether there is a threshold in the

electric field intensity required to trigger the ferroelectric transition, we repeated our simulations for several field strengths, with the results shown in FIG. 2b. Interestingly, the transition occurs only for fields greater than 1200 kV/cm. At 1100 kV/cm, the system exhibits small oscillations, while at 1000 kV/cm, it remains essentially unperturbed in its equilibrium state. This suggests that the population of finite-momentum phonons—responsible for the quantum driving force—occurs only when the system is driven far from equilibrium, thus highlighting the strongly nonequilibrium nature of the ferroelectric transition. Moreover, the time at which the transition occurs decreases with increasing electric field strength. Crucially, when the electric field is very large (5000 kV/cm), the system acquires too much kinetic energy and escapes the ferroelectric minimum.

Can the induced ferroelectricity persist indefinitely in a metastable state, or is it a transient, dynamical state doomed to fall back into the paraelectric state after a few hundred picoseconds? The answer is highly sensitive to the Born-Oppenheimer double-well PES of the FE mode. This double-well function is fully characterized by the height of the potential energy barrier,  $V_0^{FE}$ , and the position of the wells,  $x_0^{FE}$ , relative to the symmetric configuration (represented schematically in FIG. 2c). The precise values of these parameters remain uncertain, as experimental techniques are unable to measure them directly, and theoretical calculations based on density func-

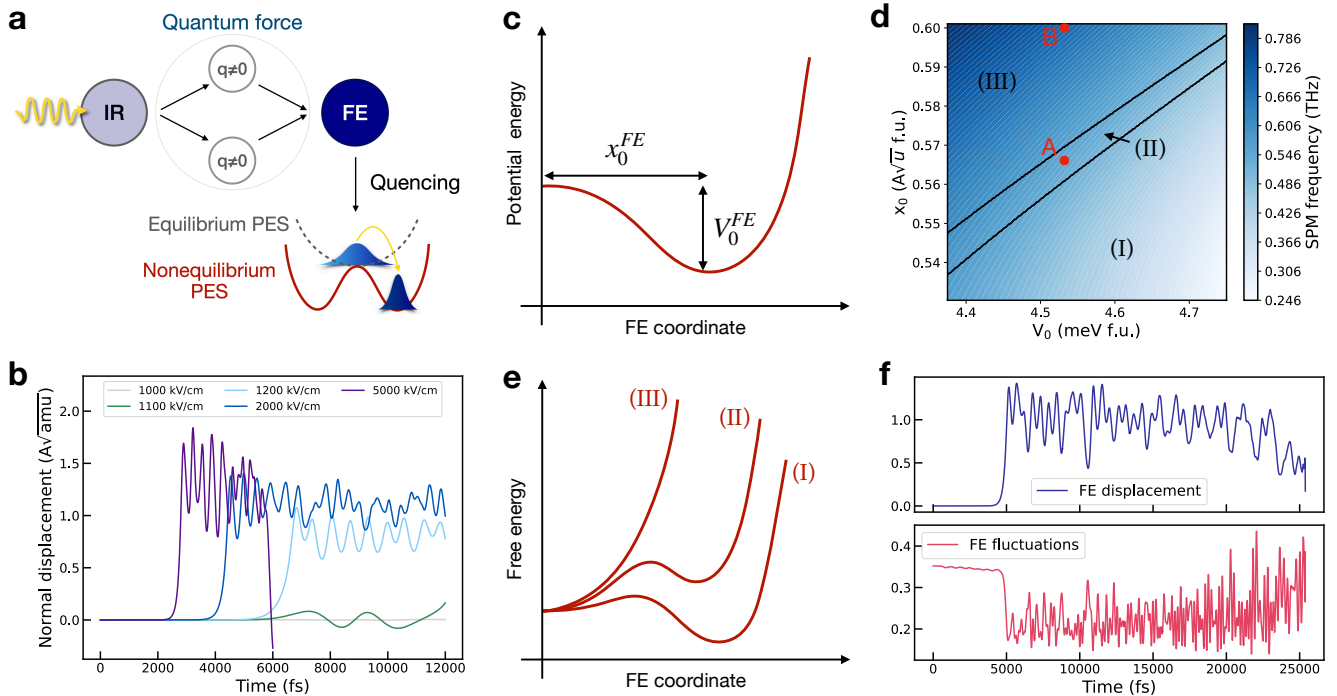


FIG. 2: **a** Schematic representation of the FE transition. **b** Electric field dependence of the FE transition. **c** Schematic representation of the double well PES of STO. **d** Map showing the FE frequency as a function of the parameters ( $V_0, x_0$ ). **e** Schematic representation of the FES shapes corresponding to regions I, II, and III in **c**. **f** FE mode displacement and fluctuations calculated at point B.

tional theory yield results that vary by an order of magnitude depending on the functional employed<sup>4</sup>. To address the presence of (meta)stable ferroelectric states, we computed the free energy landscape over a grid of  $x_0^{FE}$  and  $V_0^{FE}$  values, focusing on the parameter space where the paraelectric FE frequency lies within the experimentally relevant range (0.3–0.5 THz<sup>24,25</sup>) at 0 K (FIG. 2d). Further details are provided in the Methods section and in Section V of the Supplementary Information. We identify three distinct regions, whose corresponding energy landscapes are shown in FIG. 2e. In region (I), located in the bottom right corner of FIG. 2d, the system has a ferroelectric ground state, which contradicts experimental observations. Therefore, the parameters within this region should be excluded from consideration. It is important to emphasize that in this region, the paraelectric state is *metastable*, as evidenced by the positive frequency of the FE mode, and the two phases can coexist. The central narrow stripe (II), delimited by black solid lines, represents parameters where the paraelectric phase is the ground state, coexisting with a metastable ferroelectric phase with slightly higher energy. In contrast, in the top-left region (III), the ground state is paraelectric, and no metastable ferroelectric phase exists. Both regions (II) and (III) represent a physically acceptable parameter set. If STO at ambient pressure is in region (II), then the ferroelectric phase can survive an infinite

time; otherwise, it is doomed to fall back into the paraelectric state. While region (II) is narrow, most of the values of the FE frequency compatible with experiments are within that region.

The results presented before (FIG. 1) were obtained with a PES in region (II) (point A of FIG. 2d). To understand the expected behaviour of STO for a PES in (III) we repeated the simulation changing the interatomic potential so that the FE mode is in point B of FIG. 2d. Laser-induced atomic motion in region (III), shown in FIG. 2f, also displays a ferroelectric transition, similar to that observed in region (II). However, at longer times ( $>20$  ps), the system returns to the paraelectric configuration, highlighting the dynamical nature of the transition.

If the experimental values of  $V_0^{FE}$  and  $x_0^{FE}$  fall within the narrow region (II), this dynamic transition becomes permanent. However, if the experimental values of  $V_0^{FE}$  and  $x_0^{FE}$  are located in region (III), the induced polar order is transient. Further experimental efforts, either direct or indirect, to measure the shape of the FE potential energy surface will ultimately determine which of these scenarios is correct. The FE transition mechanism proposed in this work does not rule out the possibility that alternative mechanisms, such as the coupling of the FE mode with strain<sup>16,17</sup>, may also contribute to ferroelectric ordering, particularly when the

FE mode is directly driven by the FE pulse. However, direct evidence for this mechanism from full-atomistic simulations remains lacking.

In conclusion, through our fully atomistic quantum simulation of nonequilibrium nuclear motion, we have demonstrated a novel mechanism for ordering matter using intense laser pulses. The highest IR-active phonon, resonantly excited by light, decays into pairs of modes with finite momentum, generating a driving force on the ferroelectric mode. This process suppresses quantum fluctuations, effectively overcooling the system below its zero-temperature limit and stabilizing a classical, self-trapped ferroelectric state.

Our work provides the first demonstration that quantum fluctuations can be actively controlled with strong THz pulses to reshape the free energy landscape of a quantum system, thereby resolving the previously unexplained origin of the permanent ferroelectric transition reported in Ref. <sup>14</sup> and establishing a new framework for dynamical phase control in quantum materials.

This research was funded in part by the Swiss National Science Foundation (SNSF, Mobility fellowship P500PT\_217861) and the US National Science Foundation under Grant No. DMR-2119351. Computational resources were provided by the FAS Division of Science Research Computing Group at Harvard University.

L.M. acknowledges computational resources from CINECA, proj. IsCb8\_TDSTO

## I. METHODS

Quantum dynamics simulations are performed using the time-dependent self-consistent harmonic approximation (TD-SCHA)<sup>18,19</sup> with a recently developed exact integration scheme for ensemble averages<sup>21</sup>. This method eliminates stochastic noise<sup>20</sup>, allowing highly accurate simulations, which are essential to investigate the ferroelectric transition given the small energy difference between the paraelectric and ferroelectric phases. Additionally, it provides analytical expressions for the forces as functions of the atomic positions and the quantum fluctuation matrix. TD-SCHA assumes that the quantum density matrix of a crystal is a Gaussian in the Wigner phase-space<sup>19,26,27</sup>, parameterized by the average atomic positions  $\mathcal{R}_i$  (also called centroids) and momenta  $\mathcal{P}_i$  and the position-position, momentum-momentum and position-momentum fluctuations  $\mathcal{A}_{ij} = \langle \delta R_i \delta R_j \rangle$ ,  $\mathcal{B}_{ij} = \langle \delta P_i \delta P_j \rangle$ ,  $\Gamma_{ij} = \langle \delta R_i \delta P_j \rangle$  (see Ref.<sup>20</sup> for a complete explanation). All the variables are mass-rescaled, following the convention introduced in Ref.<sup>19</sup> (e.g.  $\mathcal{R}_i = \tilde{\mathcal{R}}_i \sqrt{m_i}$ , where  $\tilde{\mathcal{R}}_i$  is the position not rescaled by mass). The index  $i$  and  $j$  label both atoms in the supercell and Cartesian coordinates. To follow the motion of the phonon modes and their quantum fluctuations, it is often convenient to project these variables along the phonon eigenvectors  $e_{\mu i}$ , where the index  $\mu$  represents the phonon branch. This

can be done by contracting the indexes of a generic tensor  $T_{ij..k}$  with the cartesian indexes of the phonon eigenvector,  $T_{\mu\nu\dots\sigma} = T_{ij\dots k} e_{\mu i} e_{\nu j} \dots e_{\sigma k}$ . Here, the Einstein summation convention is applied, implying summation over repeated indices. For instance, the displacement of mode  $\mu$  is computed as  $\mathcal{R}_\mu = e_{\mu i} \mathcal{R}_i$ , and is illustrated in FIG. 1b for  $\mu =$  IR, FE, AFD. The diagonal component of the quantum fluctuations for the mode  $\mu$  are calculated as  $\mathcal{A}_{\mu\mu} = \mathcal{A}_{ij} e_{\mu i} e_{\mu j}$ , and shown in FIG. 1d for  $\mu =$  FE, AFD. In general, we adopt the convention that tensors with Greek indices are projected onto the phonon eigenvectors (see, for example, Eq. 2). The parameters describing the quantum state of the crystal obey the following set of differential equations.

$$\begin{cases} \dot{\mathcal{R}}_i = \mathcal{P}_i \\ \dot{\mathcal{P}}_i = \langle f_i \rangle \\ \dot{\mathcal{A}}_{ij} = \Gamma_{ij} + \Gamma_{ji} \\ \dot{\mathcal{B}}_{ik} = -\kappa_{il} \Gamma_{lj} - \kappa_{jl} \Gamma_{li} \\ \dot{\Gamma}_{ij} = \mathcal{B}_{ij} - \mathcal{A}_{il} \kappa_{lj} \end{cases} \quad (3)$$

The term  $\langle f_i \rangle$  corresponds to the ensemble average of the forces on the nuclear quantum distribution, while the term  $\kappa_{ij} = \left\langle \frac{\partial V}{\partial \mathcal{R}_i \partial \mathcal{R}_j} \right\rangle$  is the ensemble average of the curvature of the potential energy.

In the stochastic implementation of TD-SCHA<sup>20</sup>, ensemble averages are calculated using Monte Carlo sampling. While this approach is highly general, it inevitably introduces stochastic noise. Alternatively, by expanding the potential energy up to the fourth-order term, these ensemble averages can be computed analytically<sup>21</sup>, ensuring very high accuracy in time integration. The analytic expression for the ensemble averages of forces coincides with Eq. 2 of the main text, while that for the curvature is

$$\kappa_{ij} = \phi_{ij} + \chi_{ijk} \mathcal{R}_k + \frac{1}{2} \psi_{ijkl} (\mathcal{R}_k \mathcal{R}_k + A_{kl}) . \quad (4)$$

The Taylor expansion of the potential energy surface is applied to the symmetric configuration of tetragonal STO, which corresponds to the centrosymmetric  $P4/mmm$  phase. In this context, the second, third, and fourth derivatives of the potential energy surface are represented by the tensors  $\phi_{ij}$ ,  $\chi_{ijk}$ , and  $\psi_{ijkl}$ , respectively. These tensors are computed using a finite difference scheme that employs a machine-learning interatomic potential (MLIP) for STO. Details regarding the training of the MLIP can be found in Refs. <sup>17,20,28,29</sup>. It is important to emphasize that, in this exact formalism, the coordinate  $\mathcal{R}_i$  represents the displacement of atom  $i$  relative to the reference structure used for the Taylor expansion.

The lattice parameters for STO are determined through cell relaxation at 0 K, performed using SCHA in its stochastic implementation<sup>30</sup> in conjunction with the aforementioned MLIP.

Dynamic simulations are carried out on a system initially

equilibrated at 0 K. Equilibrium positions and fluctuations are obtained through SCHA relaxation. The coupling between laser light and nuclear coordinates is described by the Born effective charges, which are taken from Ref.<sup>17,20</sup> and evaluated at the equilibrium structure. These charges are assumed to remain constant throughout the simulation.

The pulse applied to the system has Gaussian shape, described by the function  $E(t) = A \cos(\omega t) e^{-\frac{t^2}{2\sigma^2}}$ , with  $A = 2$  MV/cm,  $\omega = 16.0$  THz and  $\sigma = 150$  fs. We employ an explicit Runge-Kutta method of order 5(4) for the time integration.

The parameters  $x_0^\mu$  and  $V_0^\mu$  of the potential energy surface for mode  $\mu$  are related to the diagonal components of the second- and fourth-order derivative tensors by the expressions  $x_0^\mu = \sqrt{-\frac{6\phi_{\mu\mu}}{\psi_{\mu\mu\mu}}}$  and  $V_0^\mu = \frac{3\phi_{\mu\mu}^2}{2\psi_{\mu\mu\mu}}$ . By act-

ing on these diagonal components for the mode  $\mu = \text{FE}$ , it is possible to impose the desired values of  $x_0^{\text{FE}}$  and  $V_0^{\text{FE}}$ . The detailed strategy for this modification is outlined in Ref.<sup>21</sup>. Notably, since the energy barrier of STO is on the order of a few meV, the resulting adjustments to the force constants are minimal, ensuring that all other phonon modes and their couplings remain unaffected.

The colormap in FIG. 2d is obtained by performing SCHA relaxations on a uniform grid of values  $(x_0^{\text{FE}}, V_0^{\text{FE}})$ , followed by the calculation of the free energy Hessian. The eigenvalues of this Hessian correspond to the physical frequencies of STO<sup>31</sup>. For each grid point, the FES along the FE coordinate is calculated by performing SCHA minimizations with respect to the quantum fluctuations matrix only for different displacements of the FE mode.

- 
- \* Corresponding author. [libbi@g.harvard.edu](mailto:libbi@g.harvard.edu)
- <sup>1</sup> I. Errea, M. Calandra, C. J. Pickard, J. R. Nelson, R. J. Needs, Y. Li, H. Liu, Y. Zhang, Y. Ma, and F. Mauri, *Nature* **532**, 81 (2016).
  - <sup>2</sup> I. Errea, F. Belli, L. Monacelli, A. Sanna, T. Koretsune, T. Tadano, R. Bianco, M. Calandra, R. Arita, F. Mauri, and J. A. Flores-Livas, *Nature* **578**, 66 (2020).
  - <sup>3</sup> L. Monacelli, I. Errea, M. Calandra, and F. Mauri, *Nature Physics* **17**, 63 (2021).
  - <sup>4</sup> C. Verdi, L. Ranalli, C. Franchini, and G. Kresse, *Phys. Rev. Mater.* **7**, L030801 (2023).
  - <sup>5</sup> L. Ranalli, C. Verdi, L. Monacelli, G. Kresse, M. Calandra, and C. Franchini, *Advanced Quantum Technologies* **6** (2023), 10.1002/qute.202200131.
  - <sup>6</sup> T. Esswein and N. A. Spaldin, *Phys. Rev. Res.* **4**, 033020 (2022).
  - <sup>7</sup> D. Shin, S. Latini, C. Schäfer, S. A. Sato, U. De Giovannini, H. Hübener, and A. Rubio, *Phys. Rev. B* **104**, L060103 (2021).
  - <sup>8</sup> U. Aschauer and N. A. Spaldin, *Journal of Physics: Condensed Matter* **26**, 122203 (2014).
  - <sup>9</sup> M. Fechner, M. Först, G. Orenstein, V. Krapivin, A. S. Disa, M. Buzzi, A. von Hoegen, G. de la Pena, Q. L. Nguyen, R. Mankowsky, M. Sander, H. Lemke, Y. Deng, M. Trigo, and A. Cavalleri, *Nature Materials*, 1.
  - <sup>10</sup> J. H. Haeni, P. Irvin, W. Chang, R. Uecker, P. Reiche, Y. L. Li, S. Choudhury, W. Tian, M. E. Hawley, B. Craigo, A. K. Tagantsev, X. Q. Pan, S. K. Streiffer, L. Q. Chen, S. W. Kirchoefer, J. Levy, and D. G. Schlom, *Nature* **430**, 758 (2004).
  - <sup>11</sup> M. Itoh, R. Wang, Y. Inaguma, T. Yamaguchi, Y.-J. Shan, and T. Nakamura, *Phys. Rev. Lett.* **82**, 3540 (1999).
  - <sup>12</sup> M. Takesada, M. Itoh, and T. Yagi, *Phys. Rev. Lett.* **96**, 227602 (2006).
  - <sup>13</sup> T. Mitsui and W. B. Westphal, *Phys. Rev.* **124**, 1354 (1961).
  - <sup>14</sup> T. F. Nova, A. S. Disa, M. Fechner, and A. Cavalleri, *Science* **364**, 1075 (2019), <https://www.science.org/doi/pdf/10.1126/science.aaw4911>.
  - <sup>15</sup> X. Li, T. Qiu, J. Zhang, E. Baldini, J. Lu, A. M. Rappe, and K. A. Nelson, *Science* **364**, 1079 (2019), <https://www.science.org/doi/pdf/10.1126/science.aaw4913>.
  - <sup>16</sup> D. Shin, S. Latini, C. Schäfer, S. A. Sato, E. Baldini, U. De Giovannini, H. Hübener, and A. Rubio, *Phys. Rev. Lett.* **129**, 167401 (2022).
  - <sup>17</sup> F. Libbi, A. Johansson, B. Kozinsky, and L. Monacelli, “Ultrafast quantum dynamics in srtio<sub>3</sub> under impulsive thz radiation,” (2024), arXiv:2408.12421 [cond-mat.mtrl-sci].
  - <sup>18</sup> L. Monacelli and F. Mauri, *Phys. Rev. B* **103**, 104305 (2021).
  - <sup>19</sup> A. Siciliano, L. Monacelli, G. Caldarelli, and F. Mauri, *Phys. Rev. B* **107**, 174307 (2023).
  - <sup>20</sup> F. Libbi, A. Johansson, L. Monacelli, and B. Kozinsky, *npj Computational Materials* **11**, 102 (2025).
  - <sup>21</sup> F. Libbi and B. Kozinsky, “Quantum theory of nonlinear phononics”, in preparation (2024).
  - <sup>22</sup> “Supplementary information,” Online.
  - <sup>23</sup> A. S. Disa, T. F. Nova, and A. Cavalleri, *Nature Physics* **17**, 1087 (2021).
  - <sup>24</sup> A. Yamanaka, M. Kataoka, Y. Inaba, K. Inoue, B. Hehlen, and E. Courtens, *Europhysics Letters* **50**, 688 (2000).
  - <sup>25</sup> Y. Yamada and G. Shirane, *Journal of the Physical Society of Japan* **26**, 396 (1969), <https://doi.org/10.1143/JPSJ.26.396>.
  - <sup>26</sup> E. Wigner, *Phys. Rev.* **40**, 749 (1932).
  - <sup>27</sup> K. İmre, E. Özizmir, M. Rosenbaum, and P. F. Zweifel, *Journal of Mathematical Physics* **8**, 1097 (1967), [https://pubs.aip.org/aip/jmp/article-pdf/8/5/1097/19085677/1097.1\\_online.pdf](https://pubs.aip.org/aip/jmp/article-pdf/8/5/1097/19085677/1097.1_online.pdf).
  - <sup>28</sup> J. Vandermause, S. B. Torrisi, S. Batzner, Y. Xie, L. Sun, A. M. Kolpak, and B. Kozinsky, *npj Computational Materials* **6**, 20 (2020).
  - <sup>29</sup> Y. Xie, J. Vandermause, L. Sun, A. Cepellotti, and B. Kozinsky, *npj Computational Materials* **7**, 40 (2021).
  - <sup>30</sup> L. Monacelli, R. Bianco, M. Cherubini, M. Calandra, I. Errea, and F. Mauri, *Journal of Physics: Condensed Matter* **33**, 363001 (2021).
  - <sup>31</sup> R. Bianco, I. Errea, L. Paulatto, M. Calandra, and F. Mauri, *Phys. Rev. B* **96**, 014111 (2017).